Voids and Mn-rich inclusions in a (Ga,Mn)As ferromagnetic semiconductor investigated by transmission electron microscopy

A. Kovács,[1,a] J. Sadowski,[2,3] T. Kasama,[1] J. Domagała,[3] R. Mathieu,[4] T. Dietl,[3,5] and R. E. Dunin-Borkowski[1]
[1]*Center for Electron Nanoscopy, Technical University of Denmark, Kongens Lyngby DK-2800, Denmark*
[2]*MAX-Lab, Lund University, P.O. Box 118, 221 00 Lund, Sweden*
[3]*Institute of Physics, Polish Academy of Sciences, al. Lotników 32/46, 02-668 Warszawa, Poland*
[4]*Department of Engineering Sciences, Uppsala University, P.O. Box 534, SE-751 21 Uppsala, Sweden*
[5]*Institute of Theoretical Physics, University of Warsaw, PL-00-681 Warsaw, Poland*

(Received 6 December 2010; accepted 14 March 2011; published online 29 April 2011)

Voids adjacent to cubic (ZnS-type) and hexagonal (NiAs-type) Mn-rich nanocrystals are characterized using aberration-corrected transmission electron microscopy in an annealed $Ga_{0.995}Mn_{0.005}As$ magnetic semiconductor specimen grown by molecular beam epitaxy. Nanobeam electron diffraction measurements suggest that the nanocrystals exhibit deviations in lattice parameter as compared to bulk MnAs. After annealing at 903 K, the magnetic transition temperature of the specimen is likely to be dominated by the presence of cubic ferromagnetic nanocrystals. *In situ* annealing inside the electron microscope is used to study the nucleation, coalescence, and grain growth of individual nanocrystals. © *2011 American Institute of Physics*. [doi:10.1063/1.3581108]

I. INTRODUCTION

Magnetic semiconductors are materials that can exhibit both ferromagnetic and semiconducting properties, and they are widely studied because of their intriguing physical properties and potential applications in spin-based electronic devices.[1] It has become clear in recent years[2] that the detailed identification of the atomic arrangement in such materials is indispensible for understanding their basic properties, particularly the origin of ferromagnetism. For (Ga,Mn)As that has been deposited at low temperatures, typically below 573 K, the Mn ions are known to be randomly distributed over cation[3] and interstitial sites.[4] However, in the case of postgrowth annealing[5,6] or growth at higher temperatures,[7] the Mn ions tend to aggregate into Mn-rich (Ga,Mn)As nanocrystals buried in the GaAs lattice. Such nanocrystals have been found to adopt the cubic (ZnS-type) structure of the host for annealing temperatures below 773 K.[8–10] In contrast, the precipitation of hexagonal (NiAs-type) ferromagnetic nanocrystals has been observed for higher annealing temperatures.[5,8–10] The appearance of both chemical and crystallographic phase separation is a generic property of magnetically doped semiconductors and results from the sizable contribution of open magnetic shells to the cohesive energy.[2]

For the particular semiconductor/ferromagnet nanocomposite system GaAs:MnAs, remarkable functionalities have recently been demonstrated, including enhanced magneto-optical[11] and magnetotransport[7] properties, the direct conversion of magnetization energy into electric current,[12] and an extra long spin-relaxation time in the Coulomb blockade regime.[13] A wealth of other functionalities[14,15] have been predicted for this and related systems and await experimental verification.

The characterization of nanocrystals that contain aggregated transition metal ions using transmission electron microscopy (TEM) is highly challenging, because their size and arrangement can differ little from that of the host. Although conventional bright-field phase contrast imaging has previously been used to study Mn-rich nanocrystals in GaAs layers,[5,8–10] no detailed investigations have been carried out so far. Recent improvements in the spatial resolution and chemical sensitivity of TEM techniques have resulted from the development of aberration correctors[16,17] for both TEM and scanning TEM (STEM) methods.[18] Annular dark-field (ADF) imaging in STEM, in particular, is sensitive to variations in the atomic number Z and in strain, and it also permits the acquisition of electron energy-loss spectra simultaneously with the ADF signal.[18]

Here, we use aberration-corrected TEM and aberration-corrected ADF STEM imaging to examine heat-treated $Ga_{0.995}Mn_{0.005}As$ epilayers. We show that both cubic and hexagonal Mn-rich nanocrystals can be associated with closely adjacent voids. We determine the lattice parameters of the nanocrystals using nanobeam electron diffraction (NBD). *In situ* annealing of the layers inside the microscope is used to suggest that the nanocrystals and voids may form independently. The local Mn distribution in individual nanocrystals is studied using electron energy-loss spectroscopy (EELS), and the magnetic properties of the annealed layers are discussed.

II. EXPERIMENTAL DETAILS

(Ga,Mn)As layers were grown on GaAs (001) substrates using molecular beam epitaxy (MBE) in a KRYOVAK system.[19] A high temperature GaAs buffer layer with a

[a]Author to whom correspondence should be addressed. Electronic mail: ak@cen.dtu.dk.

 © 2011 American Institute of Physics

Downloaded 06 May 2011 to 192.38.67.112. Redistribution subject to AIP license or copyright; see http://jap.aip.org/about/rights_and_permissions

thickness of 30 nm was deposited prior to (Ga,Mn)As growth. The substrate temperature was then decreased to 543 K, and 700 nm of $Ga_{0.995}Mn_{0.005}As$ were grown. As_2 dimmers were supplied from a DCA Instruments valve cracker source, operating at a stage temperature of 1173 K. The As_2/Ga flux ratio during (Ga,Mn)As growth was close to 2. After MBE growth, the samples were taken out of the vacuum system, cleaved into several pieces, and reintroduced into the MBE growth chamber for annealing in ultrahigh vacuum conditions at moderate (673 K) and high (833 and 903 K) temperatures for 60 min. Here, we concentrate on the samples that were annealed at 903 K.

Structural characterization and chemical analysis were performed on cross-sectional TEM specimens prepared using conventional mechanical polishing and Ar ion milling. The specimens were finished using low ion energies (<1 keV) in order to minimize ion beam induced sample preparation artifacts. Both image aberration-corrected and probe aberration-corrected TEM and STEM studies were carried out using FEI Titan microscopes operated at 300 kV. The inner semiangle of the ADF detector was varied between 24 and 78.4 mrad during the collection of low-angle ADF (LAADF) and high-angle ADF (HAADF) signals. Information about the local Mn concentration was obtained using a combination of ADF STEM images and EELS line-scans. A highly parallel electron beam with a 2.6 nm full-width at half maximum was used for NBD experiments. Simulated diffraction patterns were obtained using the Java version of EMS software. Thermal annealing studies were carried out *in situ* in the microscope using a heating holder. Electron diffraction patterns, ADF STEM, and bright-field (BF) TEM images were used to follow the structural and chemical changes in the specimen during annealing. The magnetic properties of the samples were studied using a superconducting quantum interference device (SQUID) magnetometer.

III. RESULTS AND DISCUSSION

Figure 1 shows representative low magnification BF STEM and ADF STEM images of the sample that had been annealed at 903 K. The images were recorded from the same area. In the BF STEM image shown in Fig. 1(a), Moiré fringes are visible at the positions of many of the nanocrystals, which are approximately equidimensional and have an average size of 10.8 nm. The nanocrystals are identified as having either cubic (ZnS-type, space group 216) or hexagonal (NiAs-type, space group 194) structures from NBD studies (see below). Adjacent to the nanocrystals are regions that have a brighter contrast than the nanocrystals themselves in the BF images. These regions exhibit dark contrast in both HAADF and LAADF STEM images recorded with different inner detector semiangles, as shown in Figs. 1(b)–1(d). The consistency of the contrast in these regions suggests that they either contain a light material or are empty. Chemical composition measurements using energy dispersive x-ray spectroscopy (not shown) and EELS (see Fig. 5) identified only Ga and As in these regions. Based on the STEM images and compositional analyses, we interpret the regions adjacent to the nanocrystals as being voids. The voids, which have

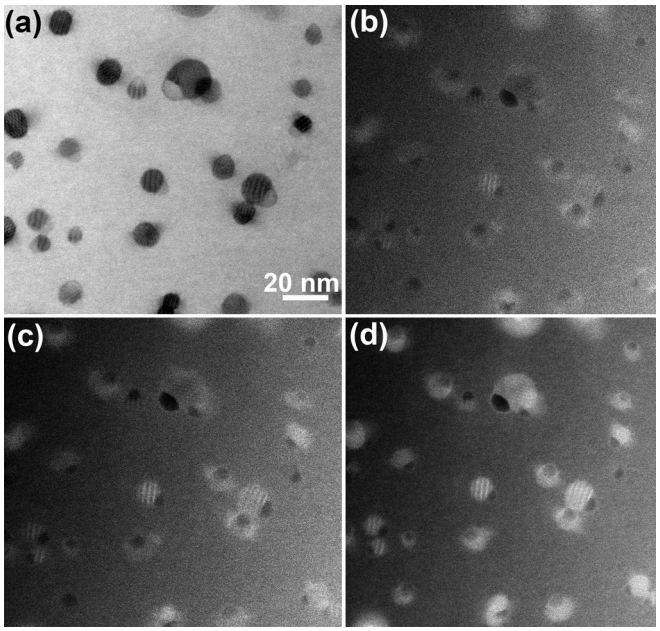

FIG. 1. Low magnification (a) bright-field STEM and (b)–(d) ADF STEM images of (Ga,Mn)As annealed at 903 K. The ADF inner detector semiangles used were (b) 78.4, (c) 47.4, and (d) 30.9 mrad. The viewing direction is close to the crystallographic [1-10] axis of the GaAs host.

bright bands of contrast around them in the LAADF image shown in Fig. 1(b), do not appear to have preferential locations or sizes with respect to the nanocrystal orientations, structures, or sizes. The origin of the bands of contrast around the voids is discussed below.

Figure 2 shows the aberration-corrected high-resolution TEM and ADF STEM images of two different cubic (Ga,Mn)As nanocrystals. To acquire the TEM images shown in Figs. 2(a) and 2(b), the objective lens aberrations were corrected up to fourth order, and a small negative value of the spherical aberration coefficient C_s (-3.5 μm) was used. At a defocus of approximately -32 nm, the GaAs host and the (Ga,Mn)As nanocrystals exhibit different contrast. The enlargement in Fig. 2(b) confirms that the nanocrystal is fully coherent with the GaAs matrix and that no dislocations are present. In such an image, an adjacent void is barely visible. Figure 2(c) shows a probe-aberration corrected HAADF STEM image of a different nanocrystal. The presence of lighter Mn atoms ($Z_{Mn}=25$, $Z_{Ga}=31$, $Z_{As}=33$) in the nanocrystal results in a slightly darker contrast than that of the GaAs host, whereas the adjacent, much darker region is a void. Interestingly, just as in Fig. 1(b), a bright rim is visible around the void in a LAADF image acquired from the same nanocrystal, as shown in Fig. 2(d). Yu *et al.*[20] showed that for a thick (>15 nm) Si sample, strain contrast can result in bright contrast in LAADF images and dark contrast in HAADF images. In a high-resolution ADF STEM image recorded from a specimen at a zone axis, channeling effects are sensitive to specimen tilt and specimen thickness. The presence of a strain field also changes the angular distributions of scattered intensity from those in a strain-free region.[20] In our studies, bands of bright contrast in LAADF images are present around both cubic and hexagonal

Downloaded 06 May 2011 to 192.38.67.112. Redistribution subject to AIP license or copyright; see http://jap.aip.org/about/rights_and_permissions

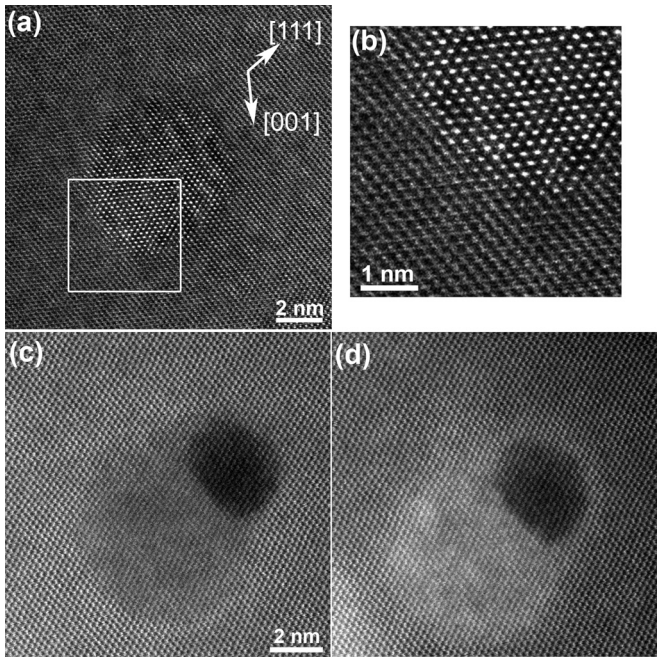

FIG. 2. High-resolution aberration-corrected (a), (b) TEM, (c) HAADF STEM, and (d) LAADF STEM images of cubic (Ga,Mn)As nanocrystals. The ADF detector inner semiangles used were (c) 78.4 and (d) 24.5 mrad.

nanocrystals and have widths of 1 to 1.5 nm, suggesting the presence of strain around the nanocrystals.

Figure 3 illustrates void formation adjacent to two different hexagonal nanocrystals. The overlapping lattices complicate the high-resolution TEM image shown in Fig. 3(a). In contrast, in the corresponding HAADF image shown in Fig. 3(b), the hexagonal lattice can be resolved, with misfit dislocations visible at the interface between the nanocrystal and the GaAs, while the void forms a sharp interface with the nanocrystal. In Fig. 3(b), a dark band of contrast is visible around the nanocrystal. Similar contrast was not as prominent around the cubic crystal shown in Fig. 2(c), presumably because of the brighter contrast of the hexagonal nanocrystal shown in Fig. 3(b) relative to that of the host GaAs lattice. The brighter contrast of the hexagonal crystal may result from either diffraction contrast or a difference in Mn concentration when compared with the cubic crystal shown in Fig. 2(c). The fact that the band around the crystals is dark in both cases suggests that it is associated with strain.

NBD was used to determine the structures and lattice parameters of individual cubic and hexagonal nanocrystals. Representative experimental and simulated diffraction patterns of cubic and hexagonal nanocrystals with diameters of 8 and 10 nm are shown in Fig. 4. The measured lattice parameter of the cubic crystal matches that of the host GaAs lattice in the (001) growth direction [Figs. 4(a) and 4(b)], whereas a smaller lattice parameter is measured in the orthogonal direction. The inferred lattice parameters for the nanocrystal of $c = 0.565$ nm and $a = 0.489 \pm 0.005$ nm are consistent with the Moiré fringes observed in Fig. 1(a) and with the separation of the 220 reflections in the diffraction pattern shown in Fig. 4(a). Despite the lattice mismatch of -13% with respect to GaAs, the lattice of the nanocrystal

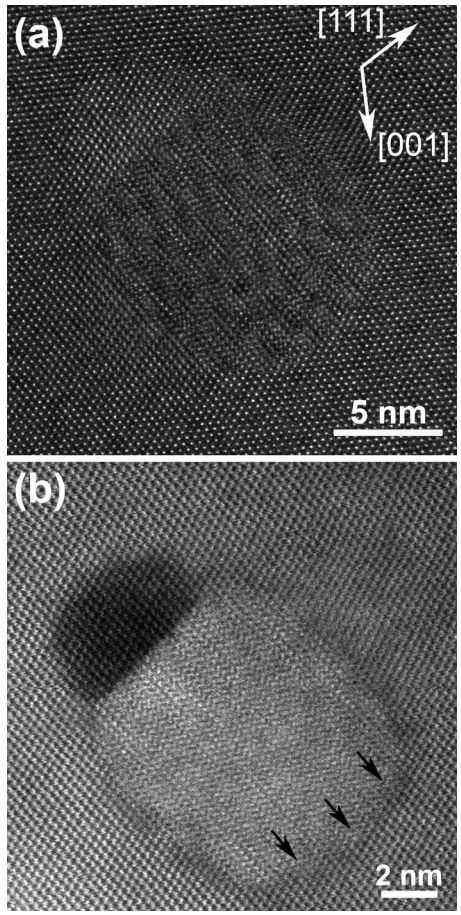

FIG. 3. Aberration-corrected high-resolution (a) TEM and (b) HAADF STEM images of two different hexagonal (Ga,Mn)As nanocrystals. The arrows indicate the positions of misfit dislocations. In (b) the inner detector semiangle used was 78.4 mrad.

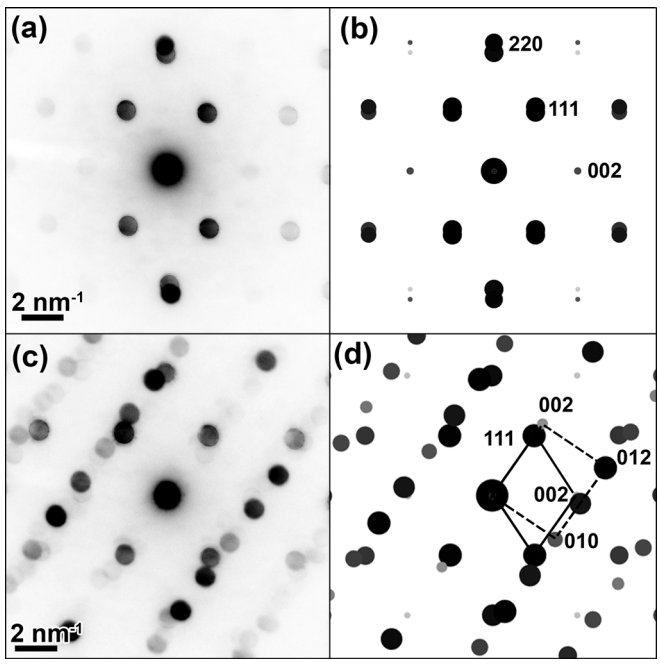

FIG. 4. (a), (c) Experimental and (b), (d) simulated electron diffraction patterns of (a), (b) cubic and (c), (d) hexagonal (Ga,Mn)As nanocrystals in GaAs. The viewing direction is [1-10] for GaAs.

Downloaded 06 May 2011 to 192.38.67.112. Redistribution subject to AIP license or copyright; see http://jap.aip.org/about/rights_and_permissions

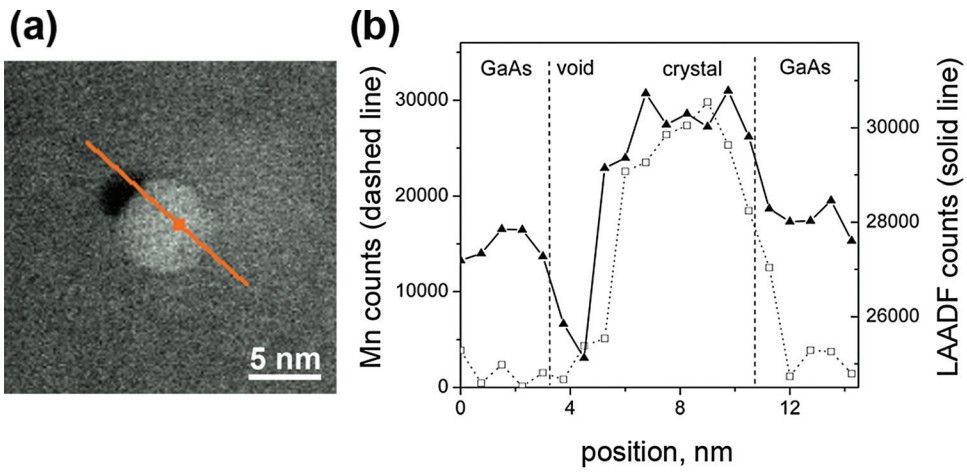

FIG. 5. (Color online) (a) LAADF (inner detector semiangle: 47.4 mrad) STEM image of a hexagonal (Ga,Mn)As nanocrystal. (b) LAADF intensity and Mn *L* edge EELS signal after background subtraction collected along the line marked in (a).

matches that of the GaAs host, as revealed in the TEM images shown in Fig. 2. The crystallographic relationship between the hexagonal nanocrystals and the GaAs lattice is determined to be $[1\text{-}10]_{GaAs}//[2\text{-}1\text{-}10]_{hex.}$, $(111)_{GaAs}//(0002)_{hex.}$ There are four possible orientations of the hexagonal *c*-axis (which is the magnetic hard axis of MnAs) with respect to the {111} planes of GaAs. By using both diffraction patterns and Fourier transform patterns of TEM lattice images (not shown), the lattice parameters of the hexagonal crystal were determined to be $a(b) = 0.359$ nm and $c = 0.589 \pm 0.005$ nm. For comparison, the bulk lattice parameters of stoichiometric MnAs are $a = 0.372$ nm and $c = 0.5713$ nm,[21] suggesting -3.5 and $+3.1\%$ strain in the *a* and *c* directions, respectively.

LAADF and EELS line-scans were recorded simultaneously in order to measure the Mn compositional profile across a hexagonal (Ga,Mn)As nanocrystal. Figure 5 shows a plot of the intensity integrated under the Mn *L* edge (640 eV), collected point-by-point across a void-nanocrystal combination in ~0.75 nm steps, plotted alongside the corresponding LAADF intensity profile. The dip in the LAADF profile corresponds to the position of the void. The Mn signal is below the detection limit of the present measurements in both the GaAs host and the void, and it increases when the electron beam reaches the nanocrystal. Interestingly, the LAADF signal increases before the Mn signal upon entering the nanocrystal from the direction of the void. The origin of this difference is not understood at present. However, it suggests that the crystal–void interface may have a different composition as compared to the interior of the crystal.

Complementary SQUID magnetometry results acquired from the same sample, which are shown in Fig. 6, are consistent with the presence of cubic Mn-rich nanocrystals, which have a higher Curie temperature ($T_C = 350$ K) than that of the NiAs-type hexagonal structure ($T_C = 313$ K).[5,7–9,19] Although we observed both structures in the samples that had been annealed at 833 K and 903 K, the temperature for magnetization onset in field-cooled measurements is determined by the magnetic nanocrystals that have the higher value of T_C.

The predominant mechanism accounting for void formation adjacent to the cubic and hexagonal nanocrystals is not fully understood. It is known that the relatively low growth temperature that is needed to incorporate a sizable concentration of Mn in GaAs (used in this study) also results in a high density of point defects, of which the most important are As antisites and Mn interstitials.[4] The annihilation of these defects during high temperature annealing may result in the formation of Mn-rich nanocrystals and vacancies. Furthermore, the process of Mn aggregation presumably proceeds via the generation of Mn vacancy–Mn interstitial pairs. Hence, heat treatment creates vacancies, the accumulation of which might than lead to the formation of voids. It is interesting to note that the presence of voids in semiconductor light emitting diodes might serve to increase their efficiency by affecting optical properties.[22]

In order to further understand the nature of void formation and Mn aggregation in GaAs, we annealed an as-grown $Ga_{0.995}Mn_{0.005}As$ sample inside the microscope and recorded LAADF images of the resulting microstructural and chemical changes, as shown in Fig. 7. The contrast of the layer in a cross-sectional specimen was uniform for annealing temperatures up to 773 K [Fig. 7(a)]. At a temperature of approximately 823 K, the formation of nanocrystals with sizes of 1 to 4 nm was observed, as shown in Fig. 7(b). The nanocrystals, which exhibited bright contrast in the LAADF images,

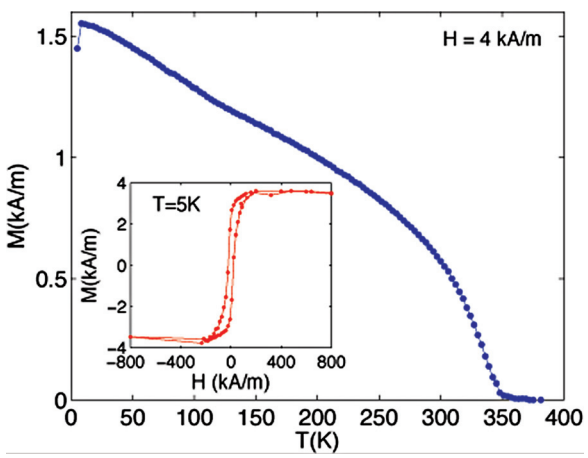

FIG. 6. (Color online) Temperature dependence of the field-cooled magnetization for $Ga_{0.995}Mn_{0.005}As$ annealed at 903 K recorded in a magnetic field of 4 kA/m (50 Oe). The inset shows a hysteresis loop acquired at $T = 5$ K (corrected by subtracting the diamagnetic contribution to the signal).

Downloaded 06 May 2011 to 192.38.67.112. Redistribution subject to AIP license or copyright; see http://jap.aip.org/about/rights_and_permissions

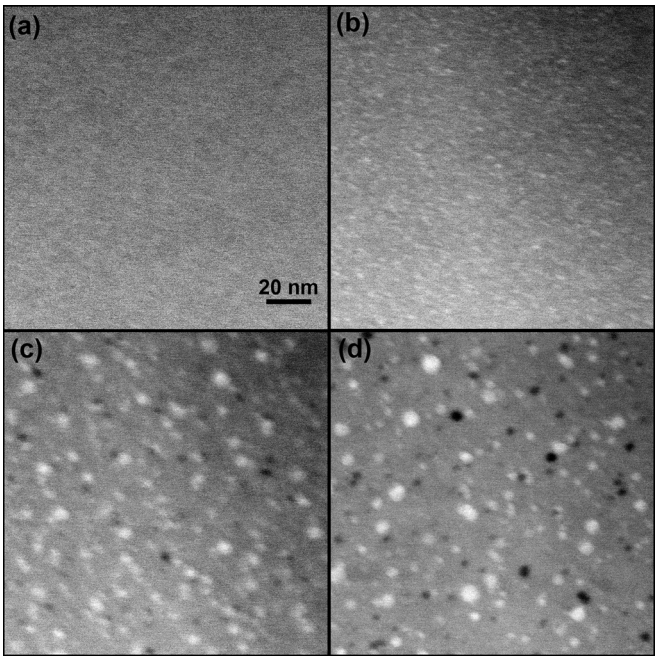

FIG. 7. LAADF (inner detector semiangle: 47.4 mrad) STEM images recorded at specimen temperatures of (a) 773, (b) 823, (c) 848, and (d) 848 K; (d) was recorded 6 min after (c).

were observed to coalesce and grow to larger sizes when the temperature was increased to 848 K [Fig. 7(c)]. Void formation was then observed at positions that did not appear to be related to the positions of the nanocrystals. When the specimen was held at this temperature, the voids became larger without changing their locations, while the nanocrystals moved, coalesced, and grew to larger sizes [Fig. 7(d)]. The final morphology of the sample that had been annealed *in situ* in the microscope was clearly different from that observed in the sample that had been annealed in ultrahigh vacuum conditions in the MBE chamber. This difference may result from the fact that the *in situ* annealing was carried out in different kinetic conditions. However, it illustrates the complexity of the processes that are involved and highlights the need for further dedicated studies of such systems under realistic conditions of elevated temperature and pressure in the TEM.

IV. CONCLUSIONS

Our results indicate that, despite many reports devoted to the GaAs:MnAs nanocomposite system and to its high temperature postgrowth annealing, the formation of Mn-rich nanocrystals with cubic and hexagonal structures is not yet fully understood. ADF STEM images reveal void formation adjacent to both cubic and hexagonal MnAs nanocrystals in the GaAs host during *ex situ* and *in situ* annealing at temperatures of up to 903 K. Bands of contrast that may be associated with strain are observed around both the nanocrystals and the voids using ADF imaging. *In situ* heating experiments in the microscope suggest that the nanocrystals and the voids may form independently, with the nanocrystal sizes, shapes, and positions evolving over time during annealing and with the voids remaining more static. Our results also suggest that the onset of the ferromagnetic properties of the annealed (Ga,Mn)As layers is determined by the presence of the cubic rather than the hexagonal nanocrystals.

ACKNOWLEDGMENTS

This work was supported by the "FunDMS" Advanced Grant of the European Research Council within the "Ideas" 7th Framework Programme of the European Commission.

[1]T. Dietl, D. D. Awschalom, M. Kaminska, and H. Ohno (eds.) Spintronics (Elsevier, Amsterdam, 2008), Vol. 82.
[2]A. Bonanni and T. Dietl, Chem. Soc. Rev. **39**, 528 (2010).
[3]H. Ohno, A. Shen, F. Matsukura, A. Oiwa, A. Endo, S. Katsumoto, and Y. Iye, Appl. Phys. Lett. **69**, 363 (1996).
[4]K. M. Yu, W. Walukiewicz, T. Wojtowicz, I. Kuryliszyn, X. Liu, Y. Sasaki, and J. K. Furdyna, Phys. Rev. B **65**, 201303 (2002).
[5]J. De Boeck, R. Oesterholt, A. Van Esch, H. Bender, C. Bruynseraede, C. Van Hoof, and G. Borghs, Appl. Phys. Lett. **68**, 2744 (1996).
[6]J. L. Hilton, B. D. Schultz, S. McKernan, and C. J. Palmstrøm, Appl. Phys. Lett. **84**, 3145 (2004).
[7]S. Ye, P. J. Klar, T. Hartmann, W. Heimbrodt, M. Lampalzer, S. Nau, T. Torunski, W. Stolz, T. Kurz, H.-A. Krug von Nidda, and A. Loidi, Appl. Phys. Lett. **83**, 3927 (2003).
[8]M. Moreno, A. Trampert, B. Jenichen, L. Däweritz, and K. H. Ploog, J. Appl. Phys. **92**, 4672 (2002).
[9]M. Yokoyama, H. Yamaguchi, T. Ogawa, and M. Tanaka, J. Appl. Phys. **97**, 10D317 (2005).
[10]A. Kwiatkowski, D. Wasik, M. Kamiánska, R. Bożek, J. Szczytko, A. Twardowski, J. Borysiuk, J. Sadowski, and J. Gosk, J. Appl. Phys. **101**, 113912 (2007).
[11]M. Tanaka, Semicond. Sci. Technol. **17**, 327 (2002).
[12]P. N. Hai, S. Ohya, M. Tanaka, S. E. Barnes, and S. Maekawa, Nature (London) **458**, 489 (2007).
[13]P. N. Hai, S. Ohya, and M. Tanaka, Nat. Nanotechnol. **5**, 593 (2010).
[14]H. Katayama-Yoshida, K. Sato, T. Fukushima, M. Toyoda, H. Kizaki, V. A. Dinh, and P. H. Dederichs, Phys. Status Solidi A **204**, 15 (2007).
[15]T. Dietl, J. Appl. Phys. **103**, 07D111 (2008).
[16]M. Haider, S. Uhlemann, E. Schwan, H. Rose, B. Kabius, and K. Urban, Nature (London) **392**, 768 (1998).
[17]K. W. Urban, Science **321**, 506 (2008).
[18]D. A. Muller, Nature Mater. **8**, 263 (2009).
[19]J. Sadowski, R. Mathieu, P. Svedlindh, M. Karlsteen, J. Kanski, Y. Fu, J. Z. Domagała, W. Szuszkiewicz, B. Hennion, D. K. Maude, R. Airey, and G. Hill, Thin Solid Films **412**, 122 (2002).
[20]Z. Yu, D. A. Muller, and J. Silcox, J. Appl. Phys. **95**, 3362 (2004).
[21]M. Tanaka, J. P. Harbison, M. C. Park, Y. S. Park, T. Shin, and G. M. Rothberg, J. Appl. Phys. **76**, 6278 (1994).
[22]C. M. Tsai, J.-K. Sheu, W.-C. Lai, M.-L. Lee, S.-J. Chang, C. S. Chang, T. K. Ko, and C. F. Shen, IEEE J. Sel. Top. Quantum Electron. **15**, 1275 (2009).

Downloaded 06 May 2011 to 192.38.67.112. Redistribution subject to AIP license or copyright; see http://jap.aip.org/about/rights_and_permissions